Supplement of Atmos. Chem. Phys., 24, 11365–11389, 2024
https://doi.org/10.5194/acp-24-11365-2024-supplement

Atmospheric Chemistry and Physics
Open Access

Supplement of

Global modeling of aerosol nucleation with a semi-explicit chemical mechanism for highly oxygenated organic molecules (HOMs)

Xinyue Shao et al.

Correspondence to: Minghuai Wang (minghuai.wang@nju.edu.cn) and Xinyi Dong (dongxy@nju.edu.cn)

Supplement

S1. Description of the Newly Added Chemical Mechanisms

Figure S1 shows a flowchart of the HOMs mechanism implemented into CAM6-Chem and Table S1 shows the main chemical reactions added into CAM6-Chem. In general, monoterpenes (including α-pinene, β-pinene, limonene and myrcene) are oxidized by OH radicals or O_3 to form MT-aRO_2 and MT-bRO_2 radicals (reactions 1-2 listed in Table S1, with only reactions involving α-pinene shown as an example). MT-bRO_2 undergo multi-step autoxidation reactions to form HOMs with 10 carbon atoms (C10-HOMs) (green arrows in Fig. S1 and reactions 3-4 in Table S1). The intermediates for the autoxidation are MT-cRO_2 and MT-HOM-RO_2. The MT-HOM-RO_2 radical represents the RO_2 radicals that undergo two or multi-step autoxidation. On the one hand, MT-HOM-RO_2 radicals are further oxidized to form C10-HOMs (reaction 8-10 in Table S1). On the other hand, all the MT-RO_2 radicals (including MT-aRO_2, MT-bRO_2, MT-cRO_2, and MT-HOM-RO_2) undergo self- and cross-reactions (orange arrows in Fig. S1) to form accretion products (C15 and C20) (reactions 5-7 in Table S1, with only reactions involving MT-aRO_2 shown as an example). The formation processes of C10-HOMs can be terminated by several oxidants (gray arrows in Fig. S1). SOA is formed via gas-particle partitioning processes of C10-HOMs, C15 and C20 (blue dashed arrows in Fig. S1).

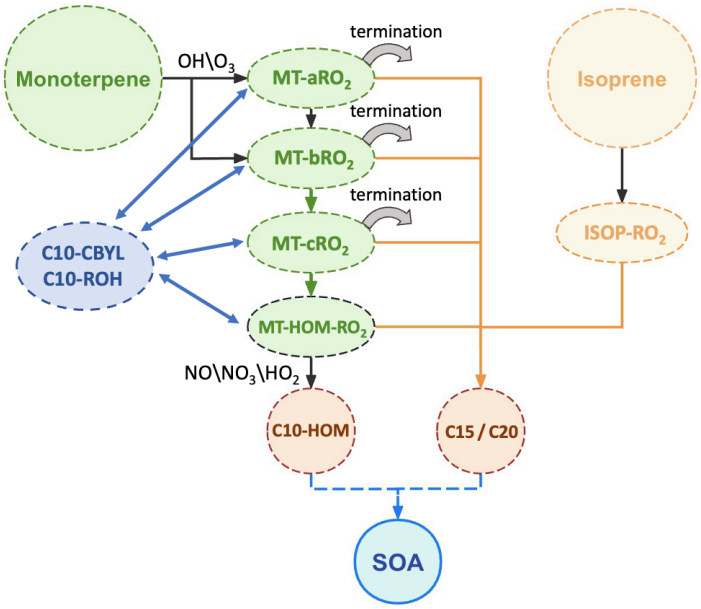

Figure S1. The flow chart of the formation and gas-particle partitioning processes of HOMs and accretion products. The green arrows represent the autoxidation reactions. The gray curved solid arrows represent the termination reactions. The yellow arrows represent the self- and cross-reactions. The blue arrows represent the conversion between C10-CBYL\C10-ROH and MT-RO2 radicals. The blue dashed arrows represent the gas-particle partitioning processes.

Table S1. Main chemical reactions added in CAM6-Chem

Index	Reactions

1	APIN + OH → 0.25*$APINO_2$ + 0.75*MT-bRO_2
2	APIN + O_3 → 0.736*$APINO_2$ + 0.064*MT-bRO_2 + 0.77*OH + 0.066*TERPA2O_2 + 0.22*H_2O_2 + 0.044*TERPA + 0.002*TERPACID + 0.034*TERPA2 + 0.17*HO_2 + 0.17*CO + 0.27*CH_2O + 0.054*TERPA2CO_3
3	MT-bRO_2 → MT-cRO_2
4	MT-cRO_2 → MT-HOM-RO_2
5	MT-aRO_2 + MT-aRO_2 → 0.893*C_{10}-CBYL + 0.29*C_{10}-ROH + 0.603*HO_2 + 1.34*HYDRALD + 0.067*MT-bRO_2 + 0.04*SOAGac20
6	MT-aRO_2 + MT-bRO_2 → 0.96*C_{10}-CBYL + 0.29*C_{10}-ROH + 0.67*HO_2 + 1.34*HYDRALD + 0.04*SOAGac20
7	MT-aRO_2 + ISOP-RO_2 → 0.4465*C_{10}-CBYL + 0.145*C_{10}-ROH + 0.145*ROH + 0.603*HO_2 + 1.485*HYDRALD + 0.0335*MT-bRO_2 + 0.04*SOAGac15
8	MT-HOM-RO_2 + HO_2 → SOAGhma + O_2
9	MT-HOM-RO_2 + NO → 0.8*NO_2 + 0.8*HO_2 + 0.4*SOAGhmb + 0.8*HYDRALD + 0.2*SOAGhmn
10	MT-HOM-RO_2 + NO_3 → HO_2 + NO_2 + 0.5*SOAGhmb + HYDRALD

Table S2. Species for HOMs and ACC formation mechanism.

Species	Molecular formula	Description
APIN [b]	$C_{10}H_{16}$	α-pinene
$APINO_2$ [b]	$C_{10}H_{17}O_3$	peroxy radical from OH +α-pinene reaction
MT-bRO_2 [a]	$C_{10}H_{16}O_4$	RO_2 from monoterpene+O_3/OH that can undergo autoxidation
MT-cRO_2 [a]	$C_{10}H_{16}O_6$	RO_2 from MT-bRO_2 autoxidation
MT-HOM-RO_2 [a]	$C_{10}H_{16}O_8$	RO_2 from MT-cRO_2 autoxidation
SOAGhma [a]	$C_{10}H_{14}O_9$	gas-phase C10 HOMs product without nitrate from HO_2 reaction
SOAGhmb [a]	$C_{10}H_{14}O_9$	gas-phase C10 HOMs product without nitrate from NO and NO_3 reaction
SOAGhmn [a]	$C_{10}H_{14}O_9N$	gas-phase C10 HOMs product with nitrate from NO reaction
SOAGac15 [a]	$C_{15}H_{18}O_7$	gas-phase C15 accretion product from isoprene-derived RO_2 (ISOP-RO_2) + MT-RO_2
SOAGac20 [a]	$C_{20}H_{32}O_8$	gas-phase C20 accretion product from MT-RO_2 + MT-RO_2
ROH [a]	C_3H_8O	lumped alcohols with more than 2 carbons
C_{10}-CBYL [a]	$C_{10}H_{17}O_3$	Carbonyl with 10 carbon atoms
C_{10}-ROH [a]	$C_{10}H_{17}O_3$	Alcohol with 10 carbon atoms
CH_2O [b]	CH_2O	formaldehyde
HO_2 [b]	HO_2	hydroperoxyl radical
H_2O_2 [b]	H_2O_2	hydrogen peroxide
HYDRALD [b]	$HOCH_2CCH_3CHCHO$	lumped unsaturated hydroxycarbonyl
TERPA [b]	$C_{10}H_{16}O_2$	aldehyde terpene product with no double bonds that contains a ring like pinonaldehyde
TERPACID [b]	$C_{10}H_{16}O_4$	carboxylic acid/peracid from TERPA
TERPA2 [b]	$C_9H_{14}O_2$	TERPA oxidation product with no double bonds that contains an aldehydic group

TERPA2O$_2$ [b]	$C_9H_{15}O_4$	TERPA peroxy radical 2nd step
TERPA2CO$_3$ [b]	$C_9H_{13}O_4$	acyl peroxy radical from TERPA2

28

S2. Ion Concentrations in CAM6-Chem

Ions are introduced to the model to simulate ion-induced NPF (Dunne et al., 2016). Specifically, we consider atmospheric ions generated by galactic cosmic rays. The ion concentrations, denoted as [$n\pm$], are computed following the equation outlined by Franchin et al. (2015):

$$[n\pm] = \frac{(k_i^2 + 4\alpha q)^{0.5} - k_i}{2\alpha} \quad (S1)$$

and q (cm^{-3} s^{-1}) represents the ion-pair production rate by galactic cosmic rays (download from: https://svn-ccsm-inputdata.cgd.ucar.edu/trunk/inputdata/atm/waccm/gcrs/). α is the ion–ion recombination coefficient (cm^3 s^{-1}) calculated by (Franchin et al., 2015):

$$\alpha = 6 \times 10^{-8} \left(\frac{300}{T}\right)^{0.5} + 6 \times 10^{-26}[M_{air}] \left(\frac{300}{T}\right)^{4} \quad (S2)$$

[M_{air}] is the concentration of air molecules (cm^{-3}). The ion loss rate k_i, is due to the ion condensation sink (CS) onto aerosols and the ion-induced nucleation:

$$k_i = CS + \frac{J_{Org,i}}{2[n\pm]} \quad (S3)$$

S3. COC Saturated Concentration in CAM6-Chem

Condensable organic compounds (COC) condense onto newly formed aerosols in accordance with their saturation vapor concentration, denoted as (C^*_{COC}). This concentration is computed using the ideal gas law equation:

$$C^*_{COC} = \frac{MW \times \zeta \times P(T)}{R\,T} \quad (S4)$$

where *MW* is the molecular weight of the COC and ζ is the activity coefficient of COC and assumed equal to 1. *P(T)* is the saturation vapor pressure at temperature *T*, *R* is the ideal gas constant. The saturation vapor pressure at temperature *T* can be calculated following Chung and Seinfeld (2002):

$$P(T) = P(T_0) \cdot e^{\left[\frac{-\Delta H_{vap}}{R}\left(\frac{1}{T}-\frac{1}{T_0}\right)\right]} \quad (S5)$$

where $P(T_0)$ is the saturation vapor pressure at temperature T_0 =298 K and ΔH_{vap} is the enthalpies of vaporization which represent the energy to transform the liquid substance into gas-phase (values shown in Table 1).

S4. Threshold Value of NPF Event Happening

To determine the threshold threshold to initiate an NPF event (i.e., the threshold of j_{20nm} in model), we collect smallest nucleation rates (at size between 5nm to 30nm) measurements in Kerminen et al. (2018). Following Kerminen et al. (2018), there are total 58 sites showing smallest nucleation rates with different backgrounds, including boreal forest, China, mountainous regions, polars, rural remote and urban regions (https://iopscience.iop.org/article/10.1088/1748-9326/aadf3c/data). Distribution of frequency of the smallest nucleation rates that instrument can detect from different stations are shown in Figure S1.

When j_{20nm} > threshold, we can compare simulated nucleation / growth rate during NPF events (Table S1), condensation sink and NPF frequency (Table S2) with measurements, even in stations where thresholds are not detectable. We chose 10th percentile (j_{20nm} = 0.054 cm^{-3} s^{-1}), median value (j_{20nm} = 0.4 cm^{-3} s^{-1}) and 90th percentile (j_{20nm} = 2.43 cm^{-3} s^{-1}) of all smallest nucleation rates (Figure S1) as the threshold individually. This helps us to quantify uncertainty in above-mentioned simulated parameters (shown in Table S1 and S2).

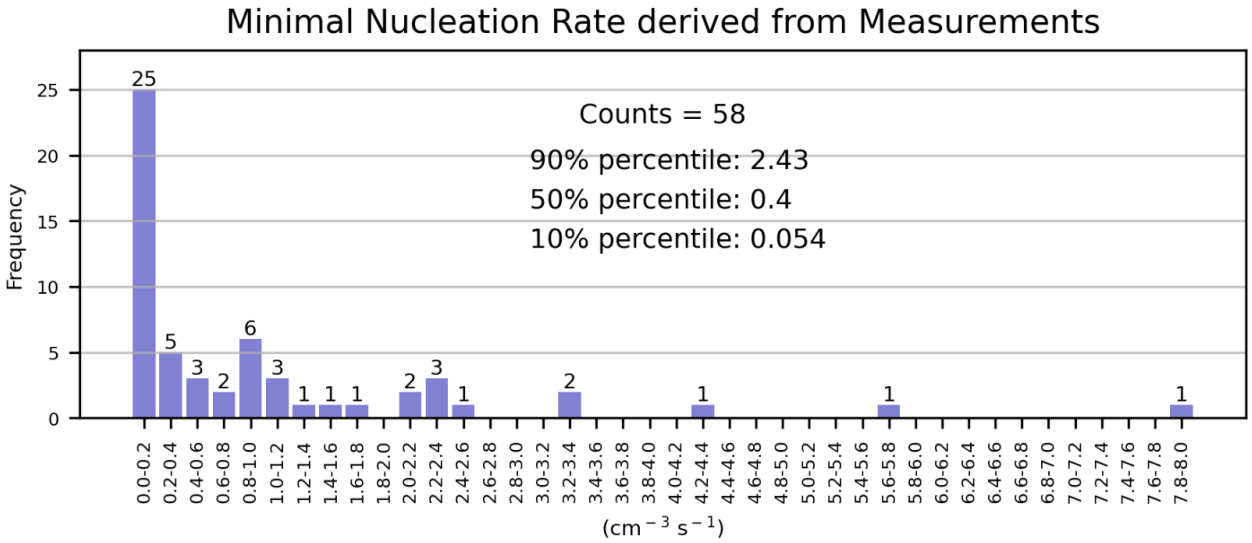

Figure S2. Frequency of smallest nucleation rate could 'start' NPF events. All the smallest nucleation rate values derived from Kerminen et al. (2018). Counts and different percentiles of all the collected nucleation rates are texted in figure.

S5. Sensitivity Test of the Loss Rate of Newly Formed Particles

In order to evaluate the uncertainty range caused by using a constant gas condensation sink (CS) instead of a size-dependent coagulation sink (CoagS) to calculate apparent nucleation rate ($j_{20\,nm}$), Eq. (8) in Lehtinen et al. (2007) was modified as follows to calculate the ratio of CS to CoagS at 1.7 nm:

$$\frac{\mathrm{CS}}{\mathrm{CoagS\ (1.7nm)}} = \left(\frac{0.71}{1.7}\right)^{-m} \tag{S6}$$

The exponent *m* has a value, depending on the background distribution, between −1 and −2. For typical atmospheric aerosols, the value of m is expected to be between −1.5 and −1.9 (Lehtinen et al., 2007) and the results of the CS/CoagS (1.7 nm) ratio using different m values are shown in Table S3.

Table S3. The ratio of the gas condensation sink (CS) to the aerosol coagulation sink at 1.7 nm (CoagS (1.7 nm)) during NPF events for different m values provided by Lehtinen et al. (2007).

m value	CS / CoagS (1.7nm)
1.5	3.63
1.6	3.98
1.7	4.40
1.8	4.91
1.9	5.51

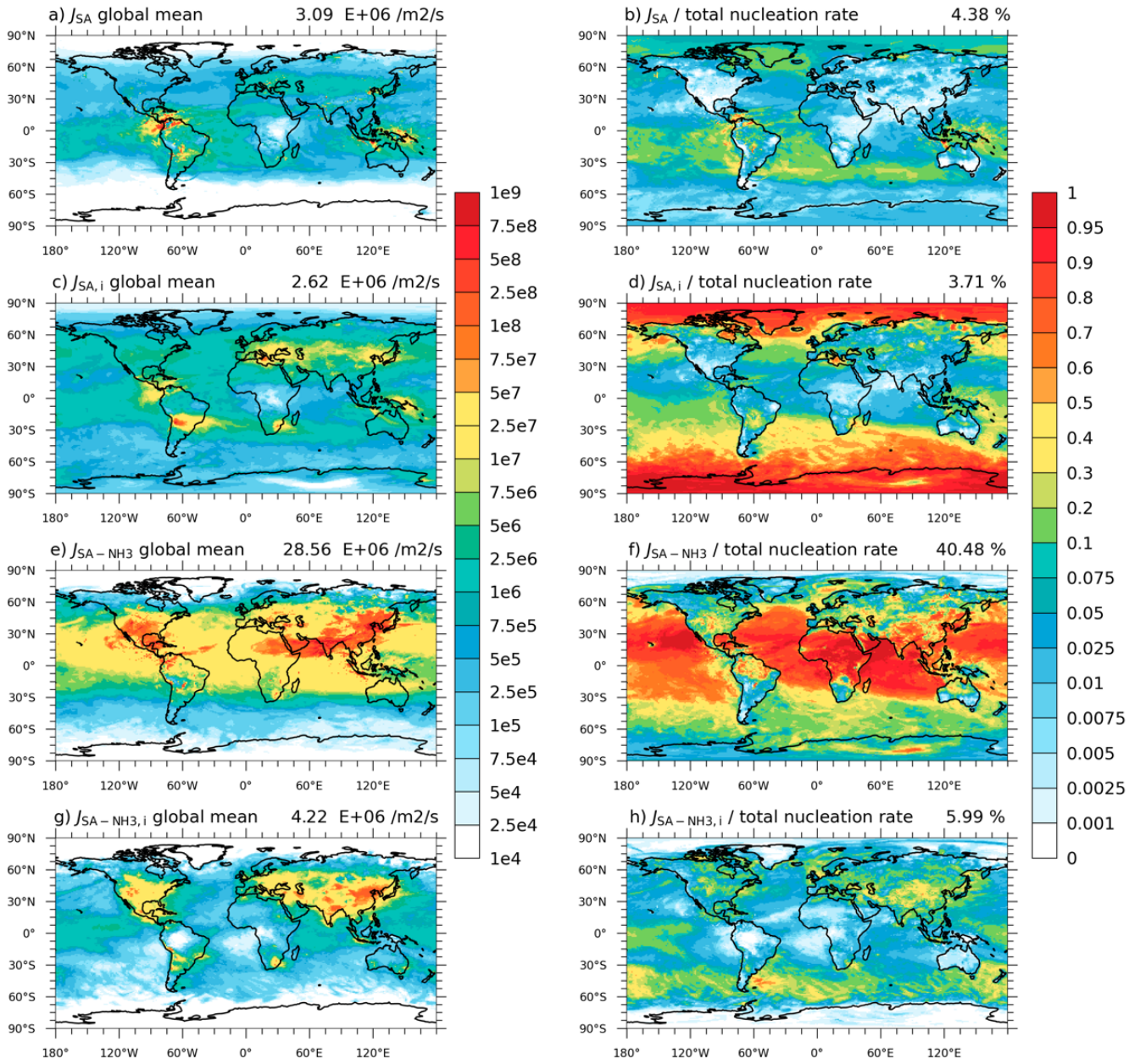

Figure S3. The 2013 annual average vertically integrated inorganic nucleation rate in the troposphere (a, c, e, g) and their contribution (b, d, f, h) for binary neutral nucleation (a, b), binary ion-induced nucleation (c, d), ternary neutral nucleation (e, f), and ternary ion-induced nucleation (g, f) for the Inorg_Org case. Global mean values are shown on the top right of each figure.

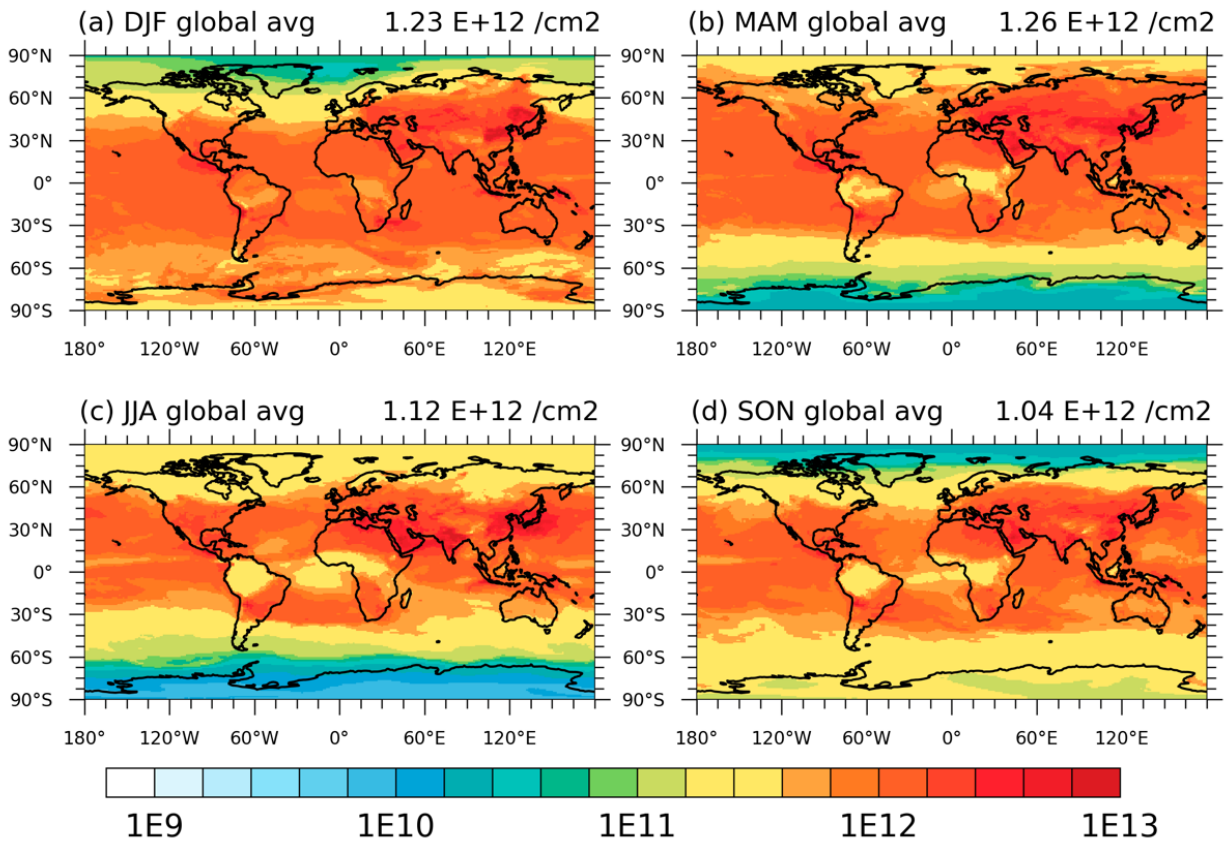

Figure S4. The 2013 annual average vertically integrated H_2SO_4 concentration for (a) DJF, (b) MAM, (c) JJA, and (d) SON in the Inorg_Org (Units: cm^{-2}). Global mean values are shown on the top right of each figure.

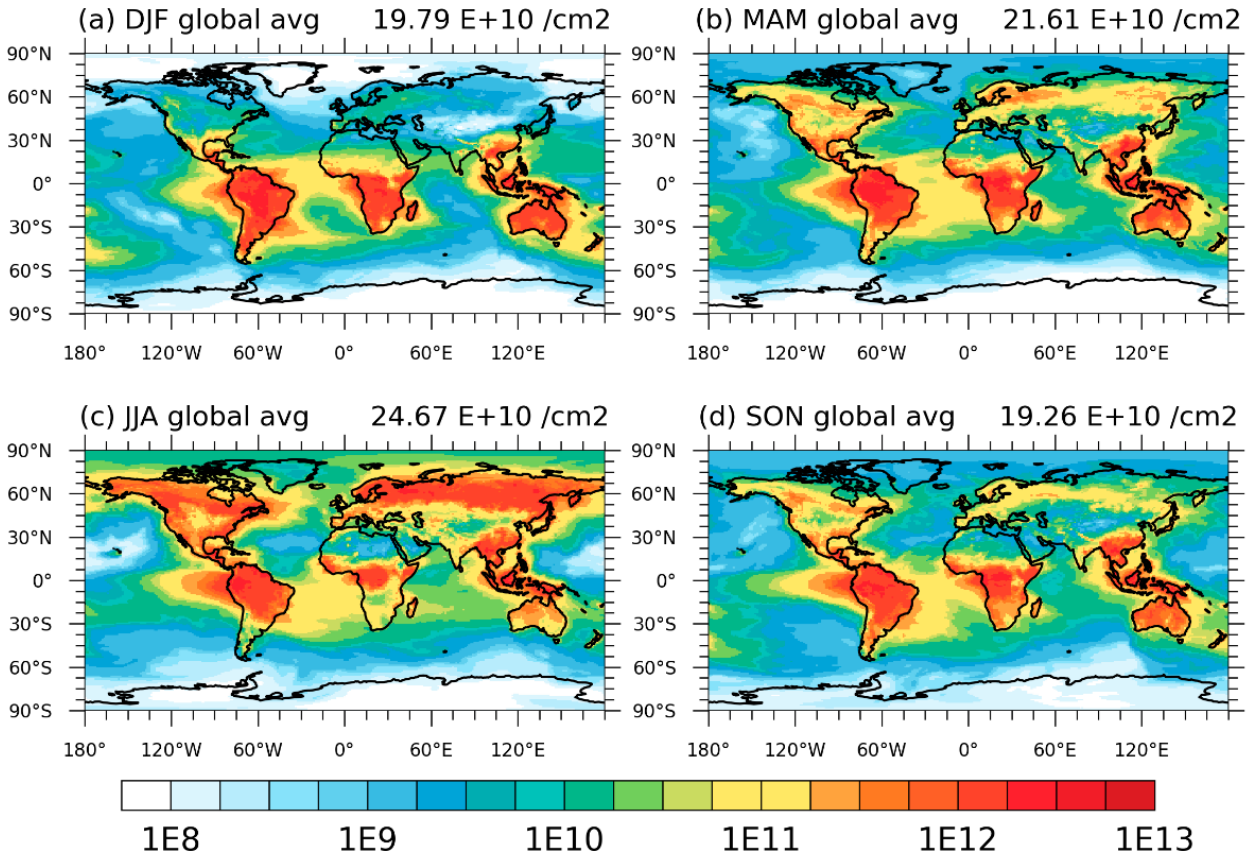

Figure S5. The 2013 annual average vertically integrated HOMs concentration for (a) DJF, (b) MAM, (c) JJA, and (d) SON in the Inorg_Org (Units: cm^{-2}). Global mean values are shown on the top right of each figure.

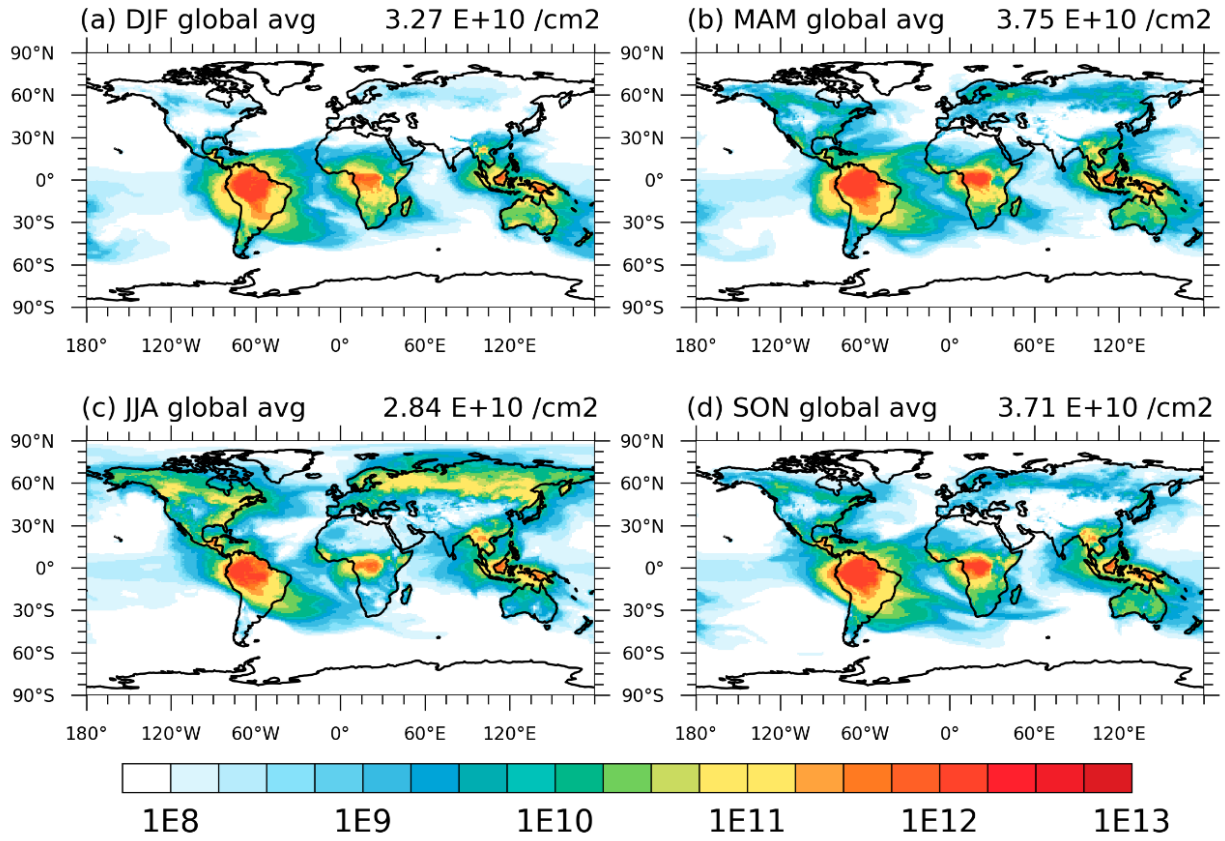

Figure S6. The 2013 annual average vertically integrated ACC concentration for (a) DJF, (b) MAM, (c) JJA, and (d) SON in the Inorg_Org (Units: cm^{-2}). Global mean values are shown on the top right of each figure.

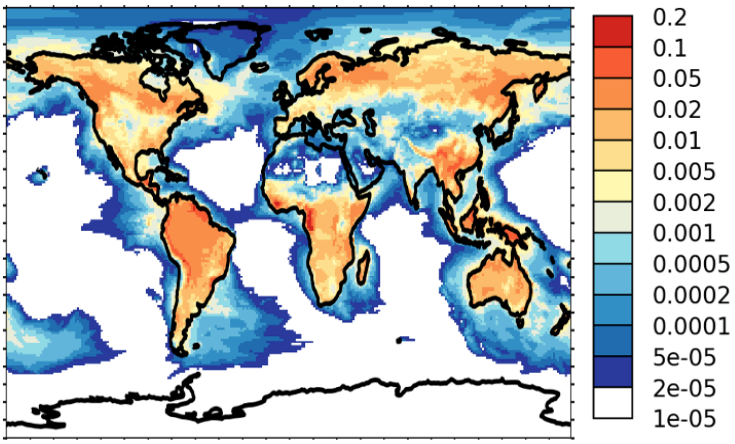

Figure S7. Annually averaged concentrations of HOMs at the top of boundary layer concentrations in this study in 2013 (scaled by 1/10) (Units: pptv).

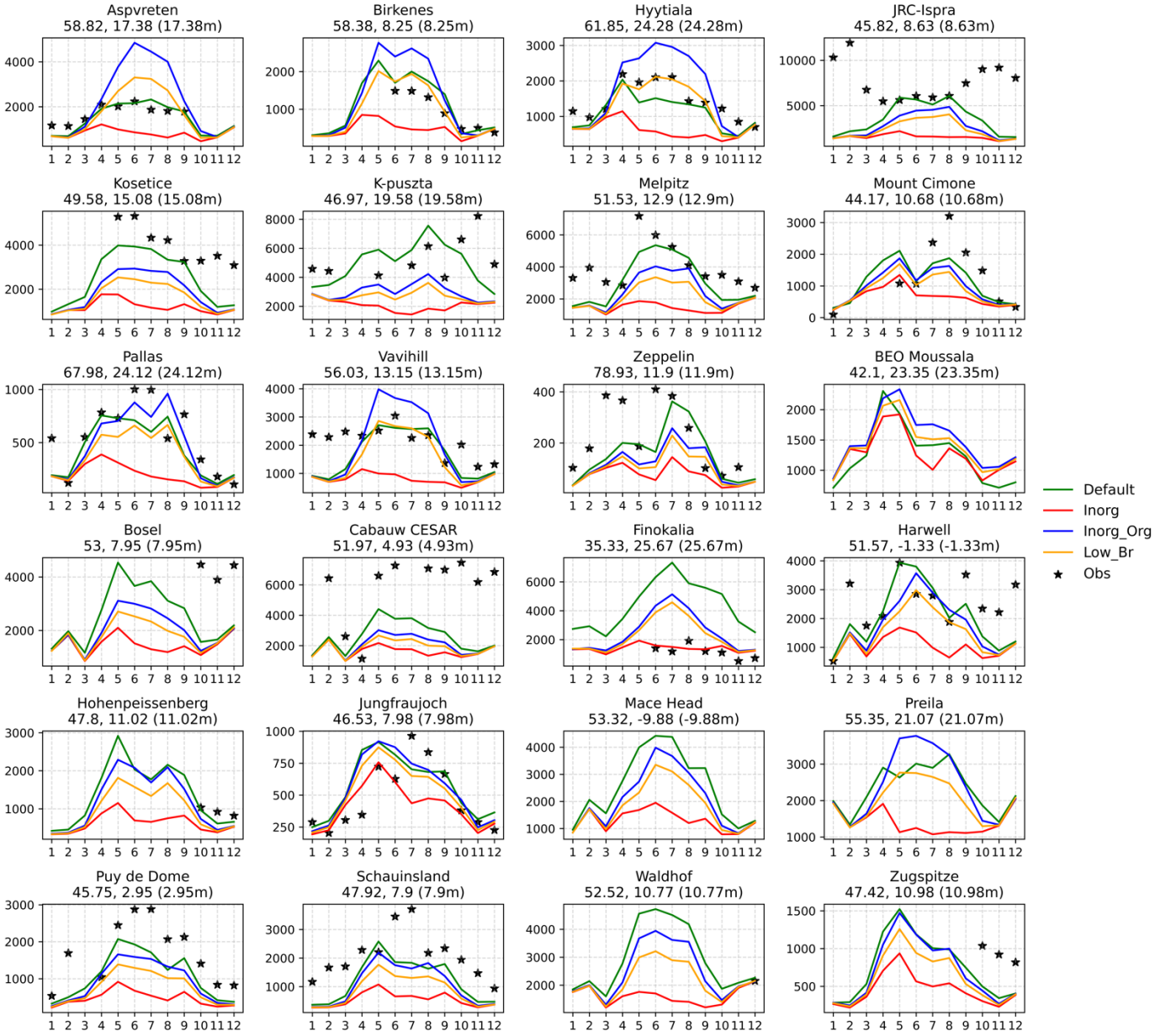

Figure S8. Seasonal cycle of N30 in 2008 at EUARCCI measurement sites (Units: cm^{-3}). The subtitle indicates site locations. Solid stars represent measured monthly mean concentrations. Numbers in X-axis show the month. Model experiments are detailed in Table 2. The red line depicts the default CESM2.1 model (Default), the yellow line indicates the model with an updated inorganic nucleation scheme (Inorg), blue lines represent the model incorporating organic nucleation based on Inorg (Inorg_Org), and orange lines are similar to blue lines but utilize a lower mass yield for nucleating organics (Low_Br).

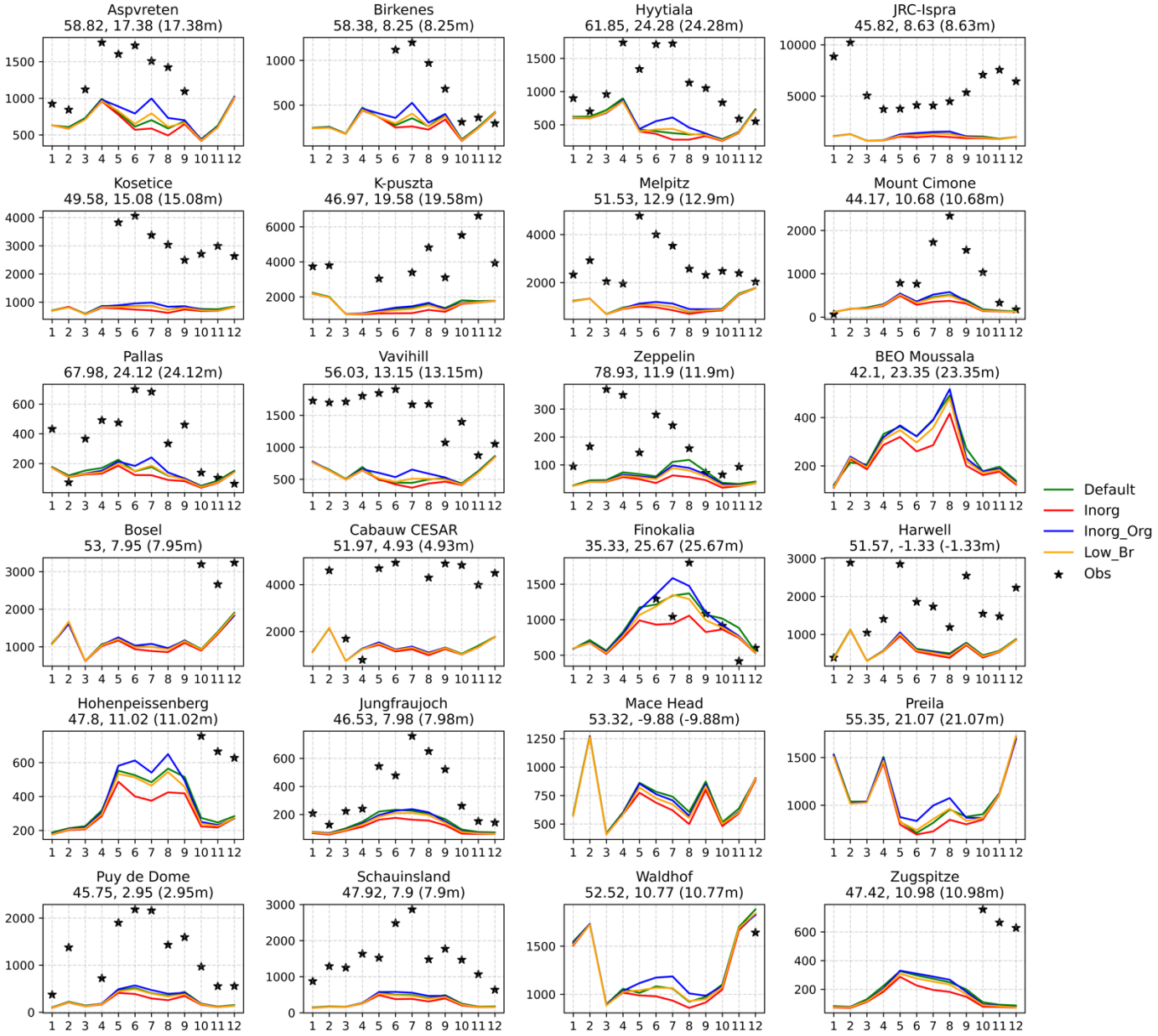

Figure S9. Same as Figure S6, but for N50 (unit: cm^{-3})

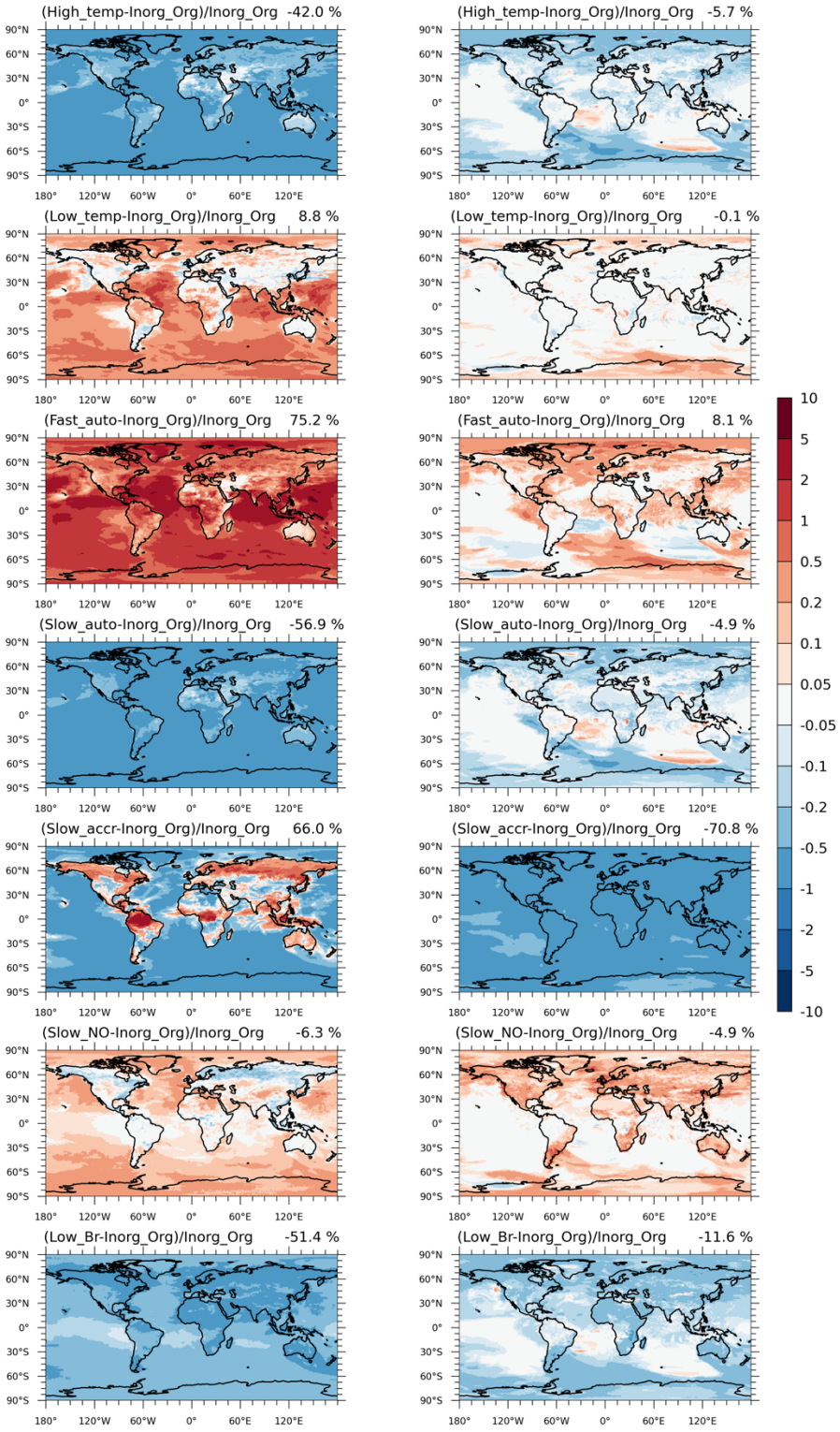

Figure S10. Relative differences (Units: unitless) of vertically-integrated HOMs (left column) and accretion products (right column) in July 2013 between Inorg_Org and other sensitivity tests. Global mean values are shown on the top right of each figure. Model experiments are described in Table 2.

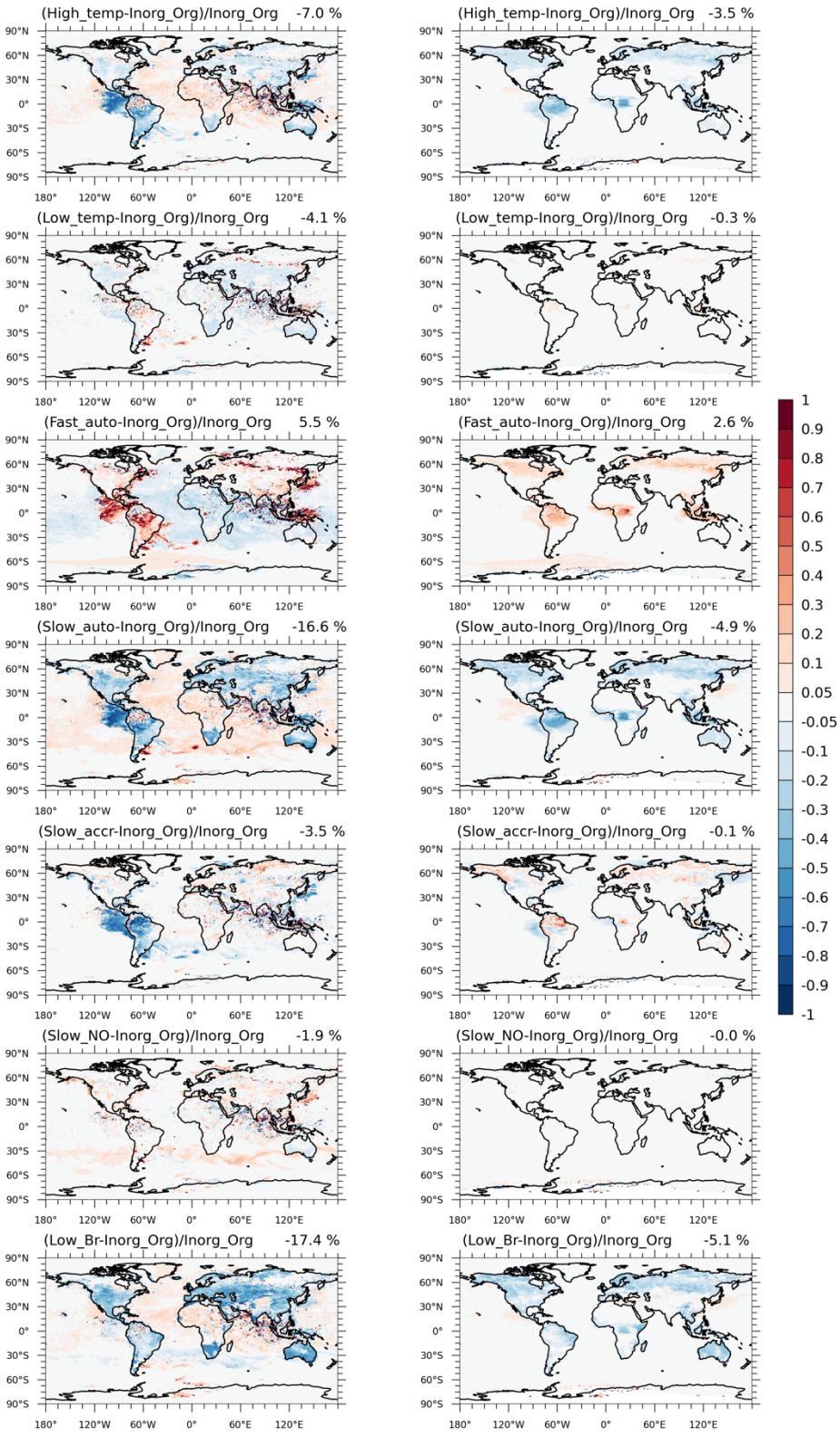

Figure S11. Relative differences (Units: unitless) of vertically-integrated nucleation (left column) and growth rate (right column) in July 2013 between Inorg_Org and other sensitivity tests. Global mean values are shown on the top right of each figure. Model experiments are described in Table 2.

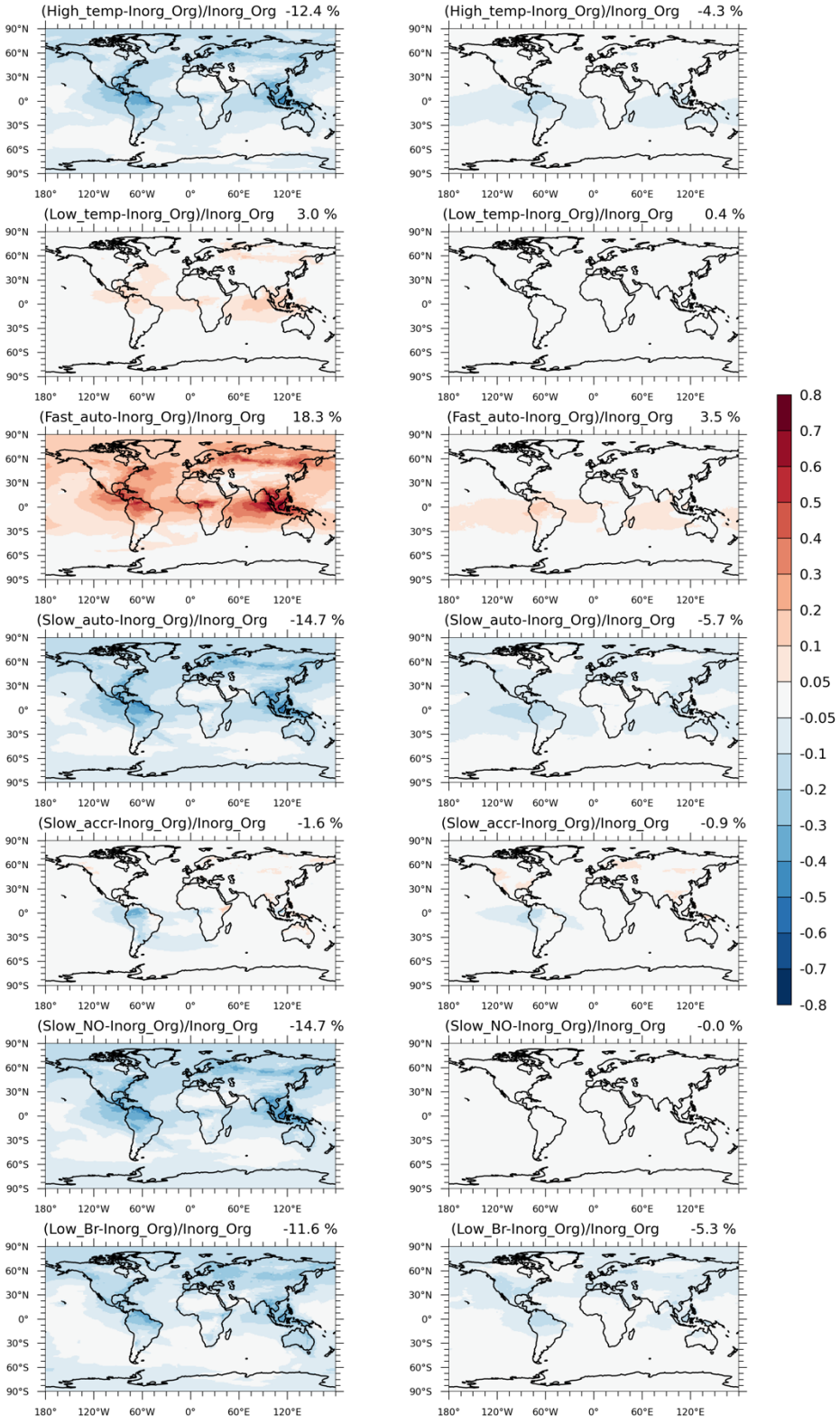

Figure S12. Relative differences (Units: unitless) of vertically-integrated aerosol (a, c, e, g, I and k) and CCN number concentration (b, d, f, h, j and l) in July 2013 between Inorg_Org and other sensitivity tests. Global mean values are shown on the top right of each figure. Model experiments are described in Table 2.

Table S4. Results of model simulations conducted at 13 different sites, based on the experimental configurations outlined in Table 2.

Date	Station[c]	Location	Type	Nucleation Rate (J) (/cm3/s)			Size for J (nm)	Growth Rate (GR) (nm/h)			Size range for GR (nm)
				Obs[a]	Inorg_Org[b]	Inorg[b]		Obs[a]	Inorg_Org[b]	Inorg[b]	
03-04/2007	Hyytiälä, Finland	61.51° N, 24.17° E (181m)	Boreal	1.08±1.05	2.4 ~ 4.3 (2.6)	0.3 ~ / (0.8)	[3, 40]	2.76±0.9	7.4~11.9 (8.1)	3.0~/ (3.8)	[3, 40]
08-10/2012	Ozark Forest, US	38.74° N, 92.20° W (3.7m)	Forest	11±10.6	5.3 ~ 10.8 (6.1)	0.4 ~ / (0.9)	1	4.7±2.6	5.6~6.8 (6.0)	5.9 ~ / (5.4)	[5, 25]
06/2012	Po Valley, Italy	44.39° N, 11.37° E (11m)	Rural	6.8 (2.7~38.5)	3.0 ~ 4.2 (3.1)	/	[2.7, 38.5]	7.2 (3.8~13.8)	10.7~14.3 (11.1)	/	[7, 20]
03-06/2014	Leicester, UK	52° 37' N, 1° 07' W	Urban	1.335	2.7 ~4.5 (3.0)	0.3 ~ / (0.8)	[10, 25]	1.3±0.4	6.2~7.8 (6.5)	8.2~/ (9.8)	[10, 25]
08/2007	Toronto, Canada	43° 42′ N, 79° 32′ W	Semi-urban	12.9	8.2 ~ 14.4 (9.2)	0.2 ~ / (0.9)	[5.6, 30]	6.3±1.6	8.6~9.5 (9.0)	13.7 ~ / (12.6)	[5.6, 30]
04-07/2012	Gadanki, India	13.46° N, 79.17° E (375m)	Semi-urban	1.2±2.3	1.2 ~ / (1.6)	/	[5, 25]	4.1±2	5.5~/ (5.8)	/	[5, 25]
09-11/2015	Nanjing, China	32.30° N, 118.72° E	Urban	7±3.89	1.6 ~ / (2.5)	/	[5,10]	6.2±2.6	10.5~/ (12.1)	/	[10, 20]
06-07/2014	Wangdu, China	38.67° N, 115.21° E	Rural	24.6±22.8	3.2 ~ 7.5 (4.1)	/	[3, 25]	7.3±3.3	9.7~13.1 (10.7)	/	[3, 25]
07/2008	Beijing, China	39.56° N, 116.19° E (35 m)	Urban	No Obs	5.9 ~ / (7.0)	0.1 ~ / (/)	1.7	6.9±2.7	12.9~11.2 (13.9)	29.7~/ (/)	[12, 550]
01-03/2012	Nanjing, China	32.12° N, 118.95° E	Urban	23.9 (2.6-56.8)	0.5 ~ / (/)	0.4 ~ / (/)	2	5.9 (6.1-10.9)	5.3~/ (/)	4.8~/ (/)	[3, 7]
04-05/2010	Qingdao, China	36° 09' N, 120° 29' E	Urban/ Coast	13.8±14.8	4.4 ~ 11.0 (5.6)	0.1 ~ / (/)	[5.6, 30]	6.4±2.2	11.2 ~ 11.4 (11.4)	10.5~ / (/)	Over the growth period
10-11/2010	Hongkong, China	22.41° N, 114.12° E (640m)	Suburban	2.95±2.1	0.3 ~ / (/)	0.3 ~ / (/)	[5.5, 10]	3.9±1.9	14.4 ~ / (/)	14.2~/ (/)	[5.5, 25]
12/2010-01/2011	Hongkong, China	22.3° N, 114.18° E (40m)	Urban	1.9±0.6	/	/	[5.5, 10]	5.2±1.6	/	/	[5.5, 10]

[a]Obs represents mean value from observation from measurements

[b]The model result is presented as a range for each site: the lower limit of the range is mean value of nucleation/growth rate during NPF event when choosing the 10th percentile of all smallest nucleation rates as the threshold (j_{20nm} = 0.054 cm^{-3} s^{-1}) of NPF event happening, while the upper limit is based on the 90th percentile. Values in brackets represent results obtained using the median as the threshold value. A forward slash ('/') indicates that no NPF events were detected in the simulation.

[c]Measurements in Hyytiälä are from Pierce et al. (2011). Measurements in Ozark forest are from Yu et al. (2014). Measurements in Po Valley are from Kontkanen et al. (2016). Measurements in Leicester are from Hama et al. (2017). Measurements in Toronto are from Meng et al. (2015). Measurements in Gadanki are from Kanawade et al. (2014). Measurements in Nanjing (2015) are from Dai et al. (2017). Measurements in Wangdu are from Wu et al. (2017). Measurements in Beijing are from Zhang et al. (2011). Measurements in Nanjing (2012) are from Herrmann et al. (2014). Measurements in Qingdao are from Zhu et al. (2014). Measurements in Hongkong (2010) are from Guo et al. (2014). Measurements in Hongkong (2010-2011) are from Wang et al. (2015).

Table S5. Comparison between measured and modeling NPF frequency and condensation sink during NPF events. Model experiments are described in Table 2.

Date	Station[d]	Location	Type	NPF Frequency (%)			Condensation Sink (s-1)		
				Obs	Inorg_Org	Inorg	Obs	Inorg_Org	Inorg
04-05/2007	Pallas, Finland	67° 58' N, 24° 07' E (560m)	Boreal forest	20	0	0	0.63	No event	No event
04-05/2007	Hyytiälä, Finland	61° 50' N, 24° 18' E (180m)	Rural, boreal forest	48	36~54 (49)	0~15 (0)	1.4	2.3 ± 1.1	No event
04-05/2007	Vavihill, Sweden	56° 01' N, 13° 09' E (172m)	Rural	57	41~61 (57)	0~13 (0)	3.4	3.2 ± 1.2	1.9 ± 1.3
04-05/2007	Mace Head, Ireland	53° 19' N, 09° 53' W (5m)	Atlantic, bare land	/	13~43 (39)	0~5 (0)	0.64	4.8 ± 1.4	1.6 ± 0.1
04-05/2007	Cabauw, Netherlands	51° 57' N, 04° 53' E (0m)	Ocean/urban	65	5~20 (18)	0~8 (0)	2.9	2.2± 0.8	1.0 ± 0.2
04-05/2007	Melpitz, Germany	51° 32' N, 12° 54' E (87m)	Rural polluted	44	11~52 (49)	0~30 (0)	8.4	5.3 ± 1.5	3.0 ± 0.8
04-05/2007	Hohenpeissenber, Germany	47° 48' N, 11° 00' E (980m)	High-elevation forest	46	0~2 (0)	0~5 (0)	4.1	No event	No event
04-05/2007	K-Puszta, Hungary	46° 58' N, 19° 35' E (125m)	Deciduous forest	83	16~79 (72)	0~40 (15)	6.6	5.6 ± 2.4	3.6 ± 1.6
04-05/2007	San Pietro Capofiume, Italy	44° 37' N, 11° 40' E (11m)	Suburban	36	60~97 (89)	0~23 (2)	4.4	4.1 ± 1.4	1.2 ± 0.3
04-05/2007	Finokalia, Greece	35° 20' N, 25° 40' E (250m)	Coastal	15	0~2 (0)	0	4.2	5.9 ± 0.1	No event
03-06/2014	Leicester, UK	52° 37' N, 1° 07' W (375m)	Urban	22	38~57 (56)	0~39 (10)	4.8 ± 1.8	2.9 ± 1.0	1.1 ± 0.4
04-07/2012	Gadanki, India	13.46° N, 79.17° E	Semi-urban	6	0~26 (22)	0	7.1±4.6	4.2 ± 0.5	1.8 ± 3.3
09-11/2015	Nanjing,China	32.30°N, 118.72°E	Urban	22	0~4 (3)	0	40 ± 25 *	14.9 ± 16.5 [c]	No event
06-07/2014	WangDu, China	38.67° N, 115.21° E	Rural	54	38~92 (88)	0	No observation		
04-05/2010	QingDao, China	36° 09' N, 120° 29' E	Urban/Coast	41	1~10 (10)	0~5 (0)	30.5 ± 12	7.6 ± 2	No event
10-11/2010	HongKong, China	22.40° N, 114.12° E (640m)	Suburban	23	0	0	50~190	3.4 ± 10.2	No event
12/2010-01/2011	HongKong, China	22.3° N, 114.18° E (40m)	Urban	20	0	0	0.63	No event	No event

[a]Obs represents mean value from observation from measurements

[b]The lower limit of the result from model simulation is derived when choosing the 10th percentile of all smallest nucleation rates as the threshold of NPF event happening, while the upper limit is based on the 90th percentile. Values in brackets represent results obtained using the median as the threshold value.

[c]The condensation sink (CS) is calculated for the entire duration of both the simulation and the measurement period, not solely during new particle formation (NPF) events.

[d]Measurements in Pallas, Hyytiälä, Vavihill, Mace Head, Cabauw, Melpitz, Hohenpeissenber, K-Puszta, San Pietro Capofiume and Finokalia are from Manninen et al. (2010).Others are tha same as Table S1.

Table S6. Comarison of sulfur budget across different studies.

		This study (CESM-MAM4)			Liu et al. (2012)		Spracklen et al. (2005)	Mann et al. (2010)
		Default	Inorg	Inorg_Org	CESM-MAM3	CESM-MAM7	GLOMAP-bin	GLOMAP-mode
Gas Burden (Tg S)	SO_2	0.29	0.29	0.29	0.35	0.34	0.49	0.3 (0.2-0.68)
	DMS	0.068	0.067	0.067	0.067	0.067	0.04	0.027 (0.02-0.15)
	H_2SO_4	0.0006	0.00059	0.00054	0.0004	0.00042		0.0001
Gas Sink (Tg S/yr)	SO_2 deposition	27.76	27.76	27.78	19.7	19		
	H_2SO_4 aqueous	0.48	0.49	0.48	0.59	0.51		
	H_2SO_4 condensation	11.61	12.018	11.89	13.9	13.7	13	
	H_2SO_4 deposition	0.0079	0.023	0.016	0.002	0.003	0.01	
	H_2SO_4 nucleation	0.37	0.11	0.17	0.03	0.03	0.07	
Gas Source	H_2SO_4 production	12.57	12.77	12.66	14.5	14.3		
H_2SO_4 lifetime (min)		24.87	24.3	22.44	14.5	15.3		

Table S7. Comarison of H_2SO_4 concentration with measurements

Measurement site	Measurement time	Coordinates	$[H_2SO_4]$ 10^6 molec cm^{-3} (>10^4)			
			Mean		Median	
			Measurement	Simulation	Measurement	Simulation
Hyytiälä, Finland	24.3.–28.6.2007	61° 51' N, 24° 17' E, 181 m a.s.l.	0.43	2.61	0.18	0.3
San Pietro Capofiume, Italy	21.6.–16.7.2009	44° 39' N, 11° 37' E, 11 m a.s.l.	5.40	4.57	2.40	2.79
Melpitz, Germany	30.4.–31.5.2008	51° 32' N, 12° 54' E, 87 m a.s.l.	6.43	10.53	2.94	2.8
Niwot Ridge, Colorado USA	24.6.–15.7.2007	40° 62' N, 105° 50' W, 3022 m a.s.l.	1.83	2.52	1.40	1.36
Atlanta, Georgia USA	30.7.–31.8.2002	33° 74' N, 84° 38' W, 275 m a.s.l.	12.90	9.95	2.85	1.03
Beijing, China	1.6–31.8.2008	four-layer building in THU 40° 94′ N, 116° 33′ E	2.51	17.91	1.81	3.15

186

Table S8. Description of sensitivity test for the autoxidation rate with different temperature dependency (Roldin et al., 2019; Weber et al., 2020).

Test Name	Reaction rate for generating	
	MT-cRO_2 (first-generation autoxidation products)	MT-HOM-RO_2 (multi-generation autoxidation products)
Low_temp	1.009E9*exp(-6000/T)	9.500E8*exp(-6000/T)
High_temp	7.768E17*exp(-12077/T)	7.311E17*exp(-12077/T)
Inorg_Org	9.800E12*exp(-8836/T)	9.800E12*exp(-8836/T)

Table S9. Description of sensitivity test for the different self-/cross- reaction rate (Weber et al., 2020; Berndt et al., 2018).

Test Name	Reaction rate for generating	
	C15	C20
Slow_accr	1.800e-12	0.400e-11
Inorg_Org	2.000~4.000e-11	4.000~26.000e-11

References

Chung, S. H. and Seinfeld, J. H.: Global distribution and climate forcing of carbonaceous aerosols, J. Geophys. Res.-Atmos., 107, 10.1029/2001jd001397, 2002.

Dai, L., Wang, H., Zhou, L., An, J., Tang, L., Lu, C., Yan, W., Liu, R., Kong, S., Chen, M., Lee, S., and Yu, H.: Regional and local new particle formation events observed in the Yangtze River Delta region, China, J. Geophys. Res.-Atmos., 122, 2389-2402, 10.1002/2016jd026030, 2017.

Franchin, A., Ehrhart, S., Leppä, J., Nieminen, T., Gagné, S., Schobesberger, S., Wimmer, D., Duplissy, J., Riccobono, F., Dunne, E. M., Rondo, L., Downard, A., Bianchi, F., Kupc, A., Tsagkogeorgas, G., Lehtipalo, K., Manninen, H. E., Almeida, J., Amorim, A., Wagner, P. E., Hansel, A., Kirkby, J., Kürten, A., Donahue, N. M., Makhmutov, V., Mathot, S., Metzger, A., Petäjä, T., Schnitzhofer, R., Sipilä, M., Stozhkov, Y., Tomé, A., Kerminen, V. M., Carslaw, K., Curtius, J., Baltensperger, U., and Kulmala, M.: Experimental investigation of ion–ion recombination under atmospheric conditions, Atmos. Chem. Phys., 15, 7203-7216, 10.5194/acp-15-7203-2015, 2015.

Guo, S., Hu, M., Zamora, M. L., Peng, J. F., Shang, D. J., Zheng, J., Du, Z. F., Wu, Z., Shao, M., Zeng, L. M., Molina, M. J., and Zhang, R. Y.: Elucidating severe urban haze formation in China, P. Natl. Acad. Sci. USA., 111, 17373-17378, 10.1073/pnas.1419604111, 2014.

Hama, S. M. L., Ma, N., Cordell, R. L., Kos, G. P. A., Wiedensohler, A., and Monks, P. S.: Lung deposited surface area in Leicester urban background site/UK: Sources and contribution of new particle formation, Atmos. Environ., 151, 94-107, https://doi.org/10.1016/j.atmosenv.2016.12.002, 2017.

Herrmann, E., Ding, A. J., Kerminen, V. M., Petäjä, T., Yang, X. Q., Sun, J. N., Qi, X. M., Manninen, H., Hakala, J., Nieminen, T., Aalto, P. P., Kulmala, M., and Fu, C. B.: Aerosols and nucleation in eastern China: first insights from the new SORPES-NJU station, Atmos. Chem. Phys., 14, 2169-2183, 10.5194/acp-14-2169-2014, 2014.

Kanawade, V. P., Tripathi, S. N., Siingh, D., Gautam, A. S., Srivastava, A. K., Kamra, A. K., Soni, V. K., and Sethi, V.: Observations of new particle formation at two distinct Indian subcontinental urban locations, Atmos. Environ., 96, 370-379, https://doi.org/10.1016/j.atmosenv.2014.08.001, 2014.

Kontkanen, J., Järvinen, E., Manninen, H. E., Lehtipalo, K., Kangasluoma, J., Decesari, S., Gobbi, G. P., Laaksonen, A., Petäjä, T., and Kulmala, M.: High concentrations of sub-3nm clusters and frequent new particle formation observed in the Po Valley, Italy, during the PEGASOS 2012 campaign, Atmos. Chem. Phys., 16, 1919-1935, 10.5194/acp-16-1919-2016, 2016.

Lehtinen, K. E. J., Dal Maso, M., Kulmala, M., and Kerminen, V.-M.: Estimating nucleation rates from apparent particle formation rates and vice versa: Revised formulation of the Kerminen–Kulmala equation, J. Aerosol Sci., 38, 988-994, https://doi.org/10.1016/j.jaerosci.2007.06.009, 2007.

Liu, X., Easter, R. C., Ghan, S. J., Zaveri, R., Rasch, P., Shi, X., Lamarque, J. F., Gettelman, A., Morrison, H., Vitt, F., Conley, A., Park, S., Neale, R., Hannay, C., Ekman, A. M. L., Hess, P., Mahowald, N., Collins, W., Iacono, M. J., Bretherton, C. S., Flanner, M. G., and Mitchell, D.: Toward a minimal representation of aerosols in climate models: description and evaluation in the Community Atmosphere Model CAM5, Geosci. Model Dev., 5, 709-739, 10.5194/gmd-5-709-2012, 2012.

Mann, G. W., Carslaw, K. S., Spracklen, D. V., Ridley, D. A., Manktelow, P. T., Chipperfield, M. P., Pickering, S. J., and Johnson, C. E.: Description and evaluation of GLOMAP-mode: a modal global aerosol microphysics model for the UKCA composition-climate model, Geosci. Model Dev., 3, 519-551, 10.5194/gmd-3-519-2010, 2010.

Manninen, H. E., Nieminen, T., Asmi, E., Gagné, S., Häkkinen, S., Lehtipalo, K., Aalto, P., Vana, M., Mirme, A., Mirme, S., Hõrrak, U., Plass-Dülmer, C., Stange, G., Kiss, G., Hoffer, A., Törő, N., Moerman, M., Henzing, B., de Leeuw, G., Brinkenberg, M., Kouvarakis, G. N., Bougiatioti, A., Mihalopoulos, N., O'Dowd, C., Ceburnis, D., Arneth, A., Svenningsson, B., Swietlicki, E., Tarozzi, L., Decesari, S., Facchini, M. C., Birmili, W., Sonntag, A., Wiedensohler, A., Boulon, J., Sellegri, K., Laj, P., Gysel, M., Bukowiecki, N., Weingartner, E., Wehrle, G., Laaksonen, A., Hamed, A., Joutsensaari, J., Petäjä, T., Kerminen, V. M., and Kulmala, M.: EUCAARI ion spectrometer measurements at 12 European sites – analysis of new particle formation events, Atmos. Chem. Phys., 10, 7907-7927, 10.5194/acp-10-7907-2010, 2010.

Meng, H., Zhu, Y., Evans, G. J., Jeong, C.-H., and Yao, X.: Roles of SO2 oxidation in new particle formation events, J. Environ. Sci., 30, 90-101, https://doi.org/10.1016/j.jes.2014.12.002, 2015.

Pierce, J. R., Riipinen, I., Kulmala, M., Ehn, M., Petäjä, T., Junninen, H., Worsnop, D. R., and Donahue, N. M.: Quantification of the volatility of secondary organic compounds in ultrafine particles during nucleation events, Atmos. Chem. Phys., 11, 9019-9036, 10.5194/acp-11-9019-2011, 2011.

Spracklen, D. V., Pringle, K. J., Carslaw, K. S., Chipperfield, M. P., and Mann, G. W.: A global off-line model of size-resolved aerosol microphysics: I. Model development and prediction of aerosol properties, Atmos. Chem. Phys., 5, 2227-2252, 10.5194/acp-5-2227-2005, 2005.

Wang, Z. B., Hu, M., Pei, X. Y., Zhang, R. Y., Paasonen, P., Zheng, J., Yue, D. L., Wu, Z. J., Boy, M., and Wiedensohler, A.: Connection of organics to atmospheric new particle formation and growth at an urban site of Beijing, Atmos. Environ., 103, 7-17, 10.1016/j.atmosenv.2014.11.069, 2015.

Wu, Z. J., Ma, N., Größ, J., Kecorius, S., Lu, K. D., Shang, D. J., Wang, Y., Wu, Y. S., Zeng, L. M., Hu, M., Wiedensohler, A., and Zhang, Y. H.: Thermodynamic properties of nanoparticles during new particle formation events in the atmosphere of North China Plain, Atmos. Res., 188, 55-63, https://doi.org/10.1016/j.atmosres.2017.01.007, 2017.

Yu, H., Ortega, J., Smith, J. N., Guenther, A. B., Kanawade, V. P., You, Y., Liu, Y., Hosman, K., Karl, T., Seco, R., Geron, C., Pallardy, S. G., Gu, L., Mikkilä, J., and Lee, S.-H.: New Particle Formation and Growth in an Isoprene-Dominated Ozark Forest: From Sub-5 nm to CCN-Active Sizes, Aerosol Sci. Technol., 48, 1285-1298, 10.1080/02786826.2014.984801, 2014.

Zhang, Y. M., Zhang, X. Y., Sun, J. Y., Lin, W. L., Gong, S. L., Shen, X. J., and Yang, S.: Characterization of new particle and secondary aerosol formation during summertime in Beijing, China, Tellus B., 63, 382-394, 10.1111/j.1600-0889.2011.00533.x, 2011.

Zhu, Y., Sabaliauskas, K., Liu, X., Meng, H., Gao, H., Jeong, C.-H., Evans, G. J., and Yao, X.: Comparative analysis of new particle formation events in less and severely polluted urban atmosphere, Atmos. Environ., 98, 655-664, https://doi.org/10.1016/j.atmosenv.2014.09.043, 2014.